

Ultrafast dynamics of heme distortion in the O₂-sensor of a thermophilic anaerobe bacterium

Olga N. Petrova^{1,5}, Byung-Kuk Yoo^{1,6}, Isabelle Lamarre¹, Julien Selles², Pierre Nioche^{3,4} & Michel Negrier^{1✉}

Heme-Nitric oxide and Oxygen binding protein domains (H-NOX) are found in signaling pathways of both prokaryotes and eukaryotes and share sequence homology with soluble guanylate cyclase, the mammalian NO receptor. In bacteria, H-NOX is associated with kinase or methyl accepting chemotaxis domains. In the O₂-sensor of the strict anaerobe *Caldanaerobacter tengcongensis* (Ct H-NOX) the heme appears highly distorted after O₂ binding, but the role of heme distortion in allosteric transitions was not yet evidenced. Here, we measure the dynamics of the heme distortion triggered by the dissociation of diatomics from Ct H-NOX using transient electronic absorption spectroscopy in the picosecond to millisecond time range. We obtained a spectroscopic signature of the heme flattening upon O₂ dissociation. The heme distortion is immediately (<1 ps) released after O₂ dissociation to produce a relaxed state. This heme conformational change occurs with different proportions depending on diatomics as follows: CO < NO < O₂. Our time-resolved data demonstrate that the primary structural event of allostery is the heme distortion in the Ct H-NOX sensor, contrastingly with hemoglobin and the human NO receptor, in which the primary structural events are respectively the motion of the proximal histidine and the rupture of the iron-histidine bond.

¹Laboratoire d'Optique et Biosciences, INSERM U1182, Ecole Polytechnique, Palaiseau, France. ²Laboratoire de Biologie du Chloroplaste et Perception de la Lumière chez les Micro-Algues, UMR 7141 CNRS-Sorbonne Université, Institut de Biologie Physico-Chimique, Paris, France. ³Laboratoire de Toxicité Environnementale, Cibles Thérapeutiques, Signalisation Cellulaire et Biomarqueurs, UMR S1124, Campus Saint-Germain-des-Prés, Université de Paris, Paris, France. ⁴Plateforme d'Analyses Moléculaires et Structurales, BioMedTech Facilities, INSERM US36 - CNRS UMS2009, Campus Saint-Germain-des-Prés, Université de Paris, Paris, France. ⁵Present address: O.N.P. Laboratoire Handicap Neuromusculaire: Physiologie, Biothérapie et Pharmacologie Appliquées, Inserm U1179, Université de Versailles Saint-Quentin-en-Yvelines, Paris, France. ⁶Present address: Department of Chemistry and Chemical Engineering, California Institute of Technology, Pasadena, CA, USA. ✉email: michel.negrier@polytechnique.edu

Dioxygen (O_2) and nitric oxide (NO) protein sensors are essential for bacteria to monitor changes of concentration of these diatomics and to adapt to new environmental conditions. Heme-based gas sensors, which are linked to various downstream functions, are present in numerous organisms, have evolved from diverse structural folds^{1,2}, and may have homologous counterparts in mammals. Particular sensors found in several bacteria species have been originally identified^{3–5} based on their sequence homology with the heme domain of the mammalian NO receptor⁶, namely the enzyme soluble guanylate cyclase (sGC). The sensing domain incorporates a *b*-type heme and was named heme nitric oxide/oxygen binding (H-NOX) domain because it may bind either O_2 or NO depending on the species, even if some H-NOX domains, including sGC, do not bind O_2 ^{7,8}. The bacterial H-NOX proteins are associated with histidine kinase or diguanylate cyclase domains in the same operon or are included in full-length proteins together with a methyl-accepting chemotaxis domain³. A subfamily of H-NOX sensors found in facultative anaerobes (such as *Shewanella oneidensis* and *Vibrio cholerae*) are specific NO sensors that do not form a stable complex with O_2 similarly with sGC. The function of such bacterial H-NOX proteins is thought to regulate biofilm formation or quorum sensing signaling in a NO-dependent manner^{9,10}. Another subfamily of H-NOX sensors was found in obligate anaerobes such as *Caldanaerobacter subterraneus* subsp. *Tengcongensis*^{7,11,12}, which lives optimally at high temperature (75–86 °C)¹¹. This sensor (named *Ct* H-NOX hereafter) shares tertiary fold with the β_1 (1–194) sensing domain of sGC, but presents a very high affinity for O_2 at room temperature^{13,14}, contrarily to sGC, the stable oxy-complex being stabilized by the distal residue Tyr140^{13,15}. Although *Ct* H-NOX sensor binds the three diatomics NO, CO, and O_2 ^{13,16}, it was proposed to act as an O_2 -sensor rather than a NO-sensor¹⁷, especially since the *Ct* H-NOX domain is fused to a methyl-accepting chemotaxis domain in a full-length protein³. However, this presumed function of the *Ct* H-NOX is not yet demonstrated by in vitro assays in correlation with bacteria living conditions, as performed for example in the case of the NO-transporter cytochrome *c*¹⁸. The detection of O_2 by H-NOX sensor in obligate anaerobes should provide these bacteria with a mechanism for metabolism adaptation or O_2 avoidance reactions.

Heme O_2 -sensors from other bacteria species, with different sequence and tertiary structures, undergo a structural rearrangement upon O_2 binding which involves the motion of particular side-chains¹⁹. Contrastingly, the static structures of *Ct* H-NOX in the Fe(II)- O_2 and Fe(III)- H_2O complexes indicated that heme

deformations could be involved in the sensing mechanism^{20–22}. Indeed, an important feature of *Ct* H-NOX is the large distortion of its heme in the Fe(II)- O_2 state^{4,5}, which departs from planarity much more than any other known heme sensors. Heme distortion is encountered in proteins with diverse folds and functions and impacts their properties^{19,23,24}, including oxidases, oxidoreductase, and cytochromes with *c*-type hemes, in which this distortion influences the redox potential. Besides this role, heme distortion could be involved in controlling the protein conformational state through interactions between the heme and the protein. For example, a heme distortion change was observed in the bacterial CooA sensor after CO binding²⁵ which activates this sensor for DNA binding. The dynamics of heme distortion change was never measured to date in any protein.

Here, we address the question of the role of the heme distortion in allostery and how the heme distortion observed in steady-state crystal structures evolves with structural dynamics. We aimed at identifying and quantifying the dynamics of heme distortion triggered by the binding to and the dissociation of diatomics from the heme of the sensor *Ct* H-NOX, focussing on its interaction with O_2 which is crucial for this anaerobe. We recorded the non-equilibrium dynamics induced by the photodissociation of O_2 and its eventual rebinding to *Ct* H-NOX using transient electronic absorption spectroscopy in the picosecond to millisecond time range to detect and to disentangle the heme structural relaxation and ligand dynamics. The behavior of the sensor in the presence of O_2 was compared to that in the presence of NO and CO in the 1 ps to 5 ns time range. These experiments revealed a unique feature of the bacterial *Ct* H-NOX sensor: the ability of immediately changing the heme distortion upon O_2 release, and consequently of modulating the molecular orbitals overlap. The heme distortion (Fig. 1) which is increased upon O_2 binding^{2,3,17} (a state that we refer to as tensed) is changed in <1 ps after O_2 dissociation to produce a relaxed state. The diatomic NO exerts a similar effect, but in a lower extent than O_2 . Conversely, the tensed state of the heme is reached after O_2 binding in <5 μ s.

Results

Due to its high affinity, the protein was directly purified as a 6-coordinated (6-c) H-NOX- O_2 complex with a characteristic Soret band maximum at 416 nm, similarly with globins²⁶, and well-separated Q-bands at 555 and 590 nm (Supplementary Fig. S1a and Table S1). The unliganded 5-coordinated (5-c) ferrous heme, generated after thorough degassing in the presence of the reductant dithionite, has a Soret at 431.5 nm whose absorption coefficient is larger than for the oxy complex. This species was used to

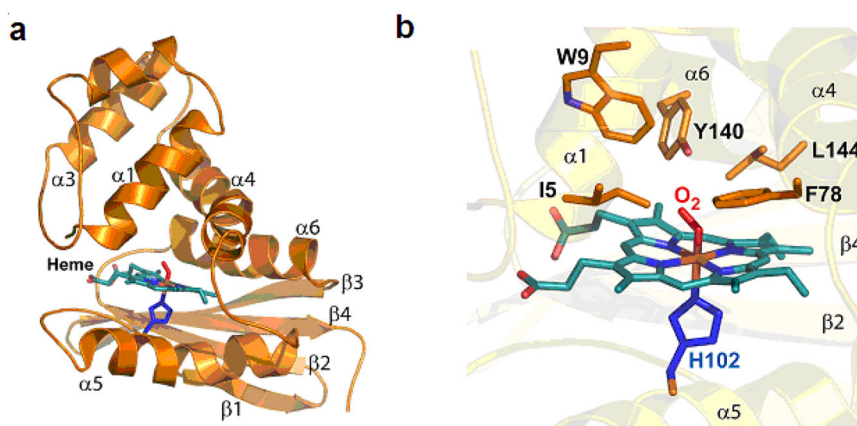


Fig. 1 Heme distortion revealed by X-ray crystal structure. **a** Overall 3D structure of the *Ct* H-NOX sensor. The heme prosthetic group is in cyan, the proximal histidine (His102) coordinating the iron in blue and the molecular oxygen in red. The figure was generated using Pymol; PDB ID: 1XBN. **b** Zoom into the heme environment and the distal amino acids surrounding the dioxygen molecule.

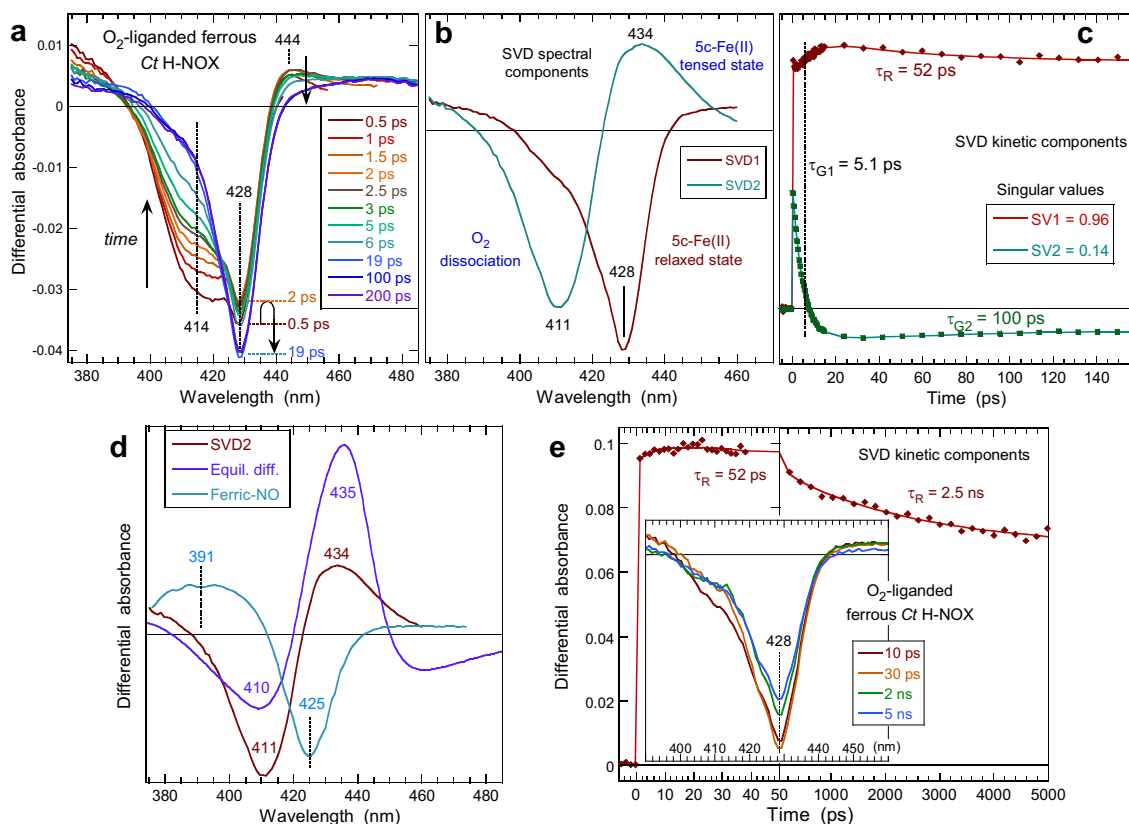


Fig. 2 Dynamics in ferrous O₂-liganded Ct H-NOX. **a** Transient difference absorption spectra (spectra at positive delay *minus* spectrum at negative delay) after the photodissociation of O₂ from ferrous heme at increasing time delay ($\lambda_{\text{ex}} = 564$ nm). **b** Spectral components from Singular Value Decomposition analysis of the time-wavelength data matrix of Ct H-NOX-O₂. **c** Associated SVD kinetic components fitted to the sum of two exponential terms and their time constants. The ordinate of the three panels is the difference of absorbance after *minus* before O₂ dissociation. SVD1 and SVD2 refer to their ranked singular values. **d** Comparison of the SVD2 spectra for the dissociation of O₂ with the equilibrium difference and the transient spectrum of NO dissociation from ferric Ct H-NOX. **e** Kinetics of the SVD1 component up to 5 ns.

prepare anaerobically the CO- and NO-liganded 6-c Ct H-NOX complexes. The spectrum of the Ct H-NOX-CO and the -NO complexes have a sharp Soret peak at 424 nm and 420 nm (Supplementary Fig. S1b and c) which have respectively larger and smaller absorption coefficients than the unliganded ferrous form. In bacterial H-NOX sensors, the proportion of 5-c-NO and 6-c-NO liganded hemes may depend upon the temperature due to the breaking of the Fe-His bond induced by NO binding, contrarily to mammalian sGC which is always 5-c-NO²⁷. The difference spectrum of Ct H-NOX-NO, which is predominantly 6-c-NO, indeed discloses a small negative shoulder at 398 nm (Supplementary Fig. S1c) which corresponds to a very small proportion of 5-c-NO species at 20 °C.

The spectrum of ferric Ct H-NOX discloses a Soret band 409 nm (Supplementary Fig. S1d) characteristic of the Fe(III)-(H₂O) species which is confirmed by the appearance of a charge transfer band at 630 nm. The 6-c-NO ferric Ct H-NOX complex is characterized by a Soret band at 424.5 nm and well-defined Q-bands at 538 and 572 nm (Supplementary Fig. S1d). These values can be compared with those of nitrophorin Fe(III)-(NO) complexes (422, 533, and 569 nm) with very similar prominent Q-bands^{28,29}. The equilibrium spectra of 6-c Ct H-NOX in the presence of coordinated diatomics are those of the samples used for time-resolved experiments.

Heme structural change induced by dioxygen dissociation from Ct H-NOX. The photodissociation of O₂ from the ferrous Ct H-NOX-O₂ complex produces an instantaneous absorption

decrease (bleaching) composed of a sharp negative band centered at 428 nm and a broad pronounced shoulder at 414 nm (Fig. 2a), whose amplitudes evolve in opposite direction during the first 20 ps. The transient spectra at early time delay are remarkably dissimilar from the difference between unliganded and O₂-liganded Ct H-NOX equilibrium spectra (Fig. 2d). Especially, no marked induced absorption band appeared at 435 nm in the transient spectra due to the unliganded ferrous heme, as observed for other ferrous proteins^{26,30,31}, but instead a very small positive band at 444–450 nm which quickly declines to a very broad and unstructured absorption spanning the 440–480 nm range (Fig. 2a) which does not correspond to the identified ferrous 5-c heme. The negative shoulder at 414 nm is assigned to the dissociation of O₂. It decreases faster than the main bleaching at 428 nm and evolves with different dynamics, as shown by the shift of the two isosbestic points when time elapses (400 and 440 nm), indicating that two different processes occur after O₂ dissociation. Importantly, the two bleachings are well resolved and evolve with different kinetics. Consequently, the respective spectral contributions associated with the two particular individual processes could be disentangled by Singular Value Decomposition (SVD)³² analysis of the data matrix (Fig. 2b, c).

The SVD1 spectral component (larger singular value), corresponding to the immediate formation of the bleaching at 428 nm and its evolution, is assigned to the disappearance of the 5-c ferrous heme distorted state immediately after O₂ dissociation, as it was at equilibrium in the presence of bound O₂¹⁷. The SVD2 spectrum of photo-excited Ct H-NOX-O₂ reveals a positive induced absorption corresponding to the 5c-Fe²⁺ heme

immediately dissociated, that is to say still distorted. It is assigned to O₂ dissociation (disappearance of 6-c Fe²⁺-O₂) and appearance of the 5-c ferrous heme, because the positive and negative absorption bands are located at the same position as in the equilibrium difference spectrum (Fig. 2d). However, the comparison between SVD2 and equilibrium difference spectra (Fig. 2d) readily reveals their dissimilarity, essentially the amplitude of the induced absorption at 435 nm. This is due to the fact that the 5-c ferrous heme is not in the same state of distortion (the SVD spectrum is the signature of a process), yet SVD analysis could retrieve the induced absorption which is contained in the data matrix, although it is not visible in the raw transient spectra (Fig. 2a), taking into consideration the entire spectral evolution. The decrease of SVD2 amplitude is thus due to geminate recombination of O₂. The 5-c ferrous heme changes its conformational state ultrafast (in <1 ps) after O₂ dissociation, which is the reason for the small absorbance at 444 nm in transient spectra (Fig. 2a), but the SVD2 spectrum has a positive induced absorption comparable to transient spectra of O₂ geminate rebinding in globins^{26,31}.

We must now interpret the SDV1 spectral component. Importantly, no induced absorption band appeared in the region 393–405 nm of SVD1 spectrum, where the 5-c ferric heme absorbs so that photo-oxidation can be discarded (see below the case of ferric-NO heme). Referring to the equilibrium difference spectra of O₂-bound Ct H-NOX (Fig. 2d), a simple O₂ dissociation should have produced a well-defined positive band at 435 nm. This is not the case for the SVD1 spectrum which comprises only pronounced deep bleaching at 428 nm which, together with the absence of induced absorption, implies that the heme absorption coefficient decreased, but keeping an absolute spectrum shape very close to that of the initially dissociated heme, without change of its redox or coordination state. The conclusion is that the structural state of the 5-c ferrous heme has changed immediately (<1 ps) after the dissociation of O₂, a ligand whose binding imposes such a constraint that the 6-c O₂-bound heme experiences a large distortion and immediately relaxes upon dissociation.

Another way to identify processes is to remove from a raw transient spectrum the contribution of the initial state which appears as a negative absorbance due to its disappearance (Fig. 2a). Removing the contribution of the initial O₂-liganded species from a difference transient spectrum implies to add its equilibrium spectrum and will make apparent only the produced states (Supplementary Fig. S2). We must note that all remaining

spectral contributions are intermediate states in the present case. When only one dissociated state is produced^{26,27,31}, removing the initial state results in the equilibrium spectrum of the produced state. Contrarily, here, once the equilibrium spectrum of O₂-liganded state is added, after having removed the negative contribution at 414 nm in the transient at 2.5 ps, the second bleaching at 428 nm remains, associated with the induced absorption at 442 nm. This positive absorption is due to the produced 5-coordinate photodissociated heme, whose relaxation induces the bleaching at 428 nm and implies a decrease of its absorption coefficient.

Alternatively to SVD, the raw data kinetics were analyzed directly (Supplementary Fig. S2c and d) yielding two or three exponential components (Supplementary Table S2). The decay with time constant $\tau_G = 5.5 \pm 0.5$ ps is preponderant ($A = 75\%$) in the absorption range of O₂-liganded species and corresponds to O₂ geminate rebinding to the heme in both distorted and relaxed states, as analyzed below. A fast component ($\tau_{R1} = \sim 1$ ps) is important at 440 nm, where the distorted dissociated heme appeared, and is preponderant at 420 nm where it relaxes. This fastest component is thus assigned to the heme structural relaxation which is an immediate consequence of O₂ dissociation, and is followed by a slower relaxation ($\tau_{R2} = 53 \pm 4$ ps).

Does photo-oxidation occur? Dissociation of NO from ferric Ct H-NOX.

The previous result means that the photodissociation of O₂ from Ct H-NOX transiently changes the ferrous heme conformation but not its redox state. Nevertheless, in order to ascertain this conclusion and to prove that 5-c ferric heme did not form, we photodissociated NO from the ferric heme, the only way to record its transient spectrum in the 5-c state since the Ct H-NOX ferric heme is 6-c with bound water in the steady-state, as indicated by its Soret band at 409 nm (Supplementary Fig. S1d). Indeed, at equilibrium most of the ferric hemes are 6-c with H₂O (or OH⁻) on the distal side, having a Soret band positioned at 403–410 nm, whereas the dissociated 5-c ferric heme discloses a broad Soret band centered at ~ 390 nm. A H₂O molecule cannot diffuse from solvent and bind to the heme in the ps time range, a process which takes place in the slower μ s time range³³. After the photodissociation of NO from ferric Ct H-NOX, bleaching appeared immediately at 425 nm together with a broad induced absorption centered at 391 nm (Fig. 3a). They both decay simultaneously without a shift of the isosbestic points and almost vanished at 200 ps, contrastingly to the bleaching observed

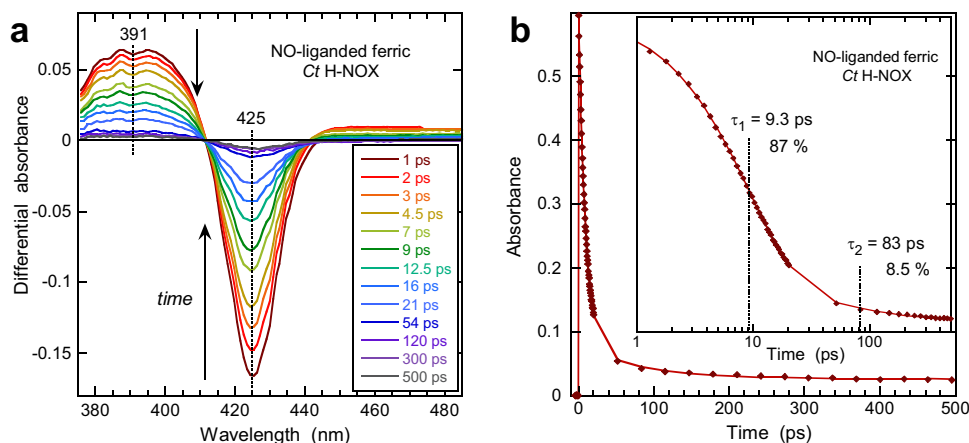


Fig. 3 Dynamics in ferric Ct H-NOX sensor. **a** Transient difference absorption spectra after the photodissociation of NO from ferric heme at increasing time delay ($\lambda_{ex} = 564$ nm). **b** Kinetics of NO geminate rebinding and fit to a sum of exponential terms (logarithmic scale in the inset) with their time constants. The constant term accounts for 4.5% of the amplitude.

for O₂-dissociated ferrous *Ct* H-NOX (Fig. 2a). The evolution of the differential spectrum is due to the geminate rebinding of NO to the ferric heme, which takes place with two-time constants ($\tau_1 = 9.3$ ps and $\tau_2 = 83$ ps, Fig. 3b) as it was observed for other ferric heme proteins interacting with NO^{33,34}. The first exponential component is due to NO rebinding from within the distal heme pocket whereas the second one is due to NO rebinding from a more distant site within the protein core. The induced absorption band at 380–400 nm decreases as NO rebinds and constitutes a marker of the 5-c unliganded ferric heme, similarly to ferric sGC³⁵ and ferric globins^{26,33}. This broad band is absent from the transient spectra of O₂-dissociated ferrous *Ct* H-NOX (Fig. 2a) firmly confirming that no photo-oxidation occurred in this latter species.

We further verified whether photo-oxidation could occur in 5-c ferrous unliganded *Ct* H-NOX by recording the heme excited states relaxation of this species (Supplementary Fig. S3 and Supplementary Results and Discussion). Electronic excited states decay and vibrational cooling of heme occurred, as similarly observed and well established for other ferrous heme proteins excited either in the Q-bands^{27,36,37} or in the Soret band^{38,39}. Importantly, the transient spectra of unliganded ferrous heme also disclose induced bleaching at 428 nm which does not reach the original baseline after 200 ps, although the heme ground state is 5-c so that no ligand can be photodissociated. Again, the absorption decrease centered at 428 nm could indicate photo-oxidation⁴⁰. However, no induced absorption band appears in the region 380–400 nm (Fig. S3a) where the 5-c ferric heme absorbs as demonstrated for Fe³⁺-NO heme (Fig. 3) and the hypothesis of photo-oxidation must be discarded in favor of a conformational change without a change of the redox state.

Dynamics of dioxygen and structural transition of *Ct* H-NOX.

The SVD1 kinetic component first discloses a rise then a slower decay (Fig. 2c). The rise is due to the O₂ rebinding ($\tau_G = 5.1$ ps) which triggers the heme structural change back to its 6-c distorted and tensed conformation (inversion of the intensity trend at the minimum of the bleaching in Fig. 2a). The heme then partly relaxes with a time constant $\tau_R = 52$ ps. The SVD2 kinetic component describes O₂ geminate rebinding in two phases, whose fast time constant (5.1 ps) is similar to constants (4.7–7.5 ps) measured in globins^{26,31,41}, in FixL and DOS bacterial O₂-sensors⁴² and in the bacterial NO-carrier cytochrome *c'* (L16A-AXCP) mutated to bind O₂³⁰, which all have tertiary folds different from *Ct* H-NOX (Supplementary Table S3). The fast kinetic phase (5.1 ps) is due to O₂ rebinding still in the heme pocket, in close vicinity to the heme iron (<5 Å) whereas the second phase is due to O₂ having migrated farther away within the protein. Similarly with myoglobin, but not with the O₂ sensors DOS and FixL, a slower phase took place ($\tau_2 = 100$ ps, $A_2 = 3$ %) which corresponds to rebinding of O₂ having diffused to a remote location in the protein. Of note, only a single O₂ geminate rebinding phase with a large amplitude has been measured for the bacterial O₂-sensors DOS and FixL (Supplementary Table S3).

When we measured the heme relaxation kinetics on a longer time scale up to 5 ns, two phases occurred with a time constant $\tau_{R1} = 52$ ps (same as in short time-range) and a second slower kinetic component with time-constant $\tau_{R2} = 2.5$ ns. They are associated with a recovery of the absorbance at 428 nm and correspond to the relaxation toward the 5-c resting state of the heme. The SVD spectral components up to 5 ns (Supplementary Fig. S4) are identical to those measured on the shorter time-scale, showing that no other process took place up to 5 ns.

The question arises as whether the reverse structural transition from relaxed to distorted heme occurs at the same time as O₂

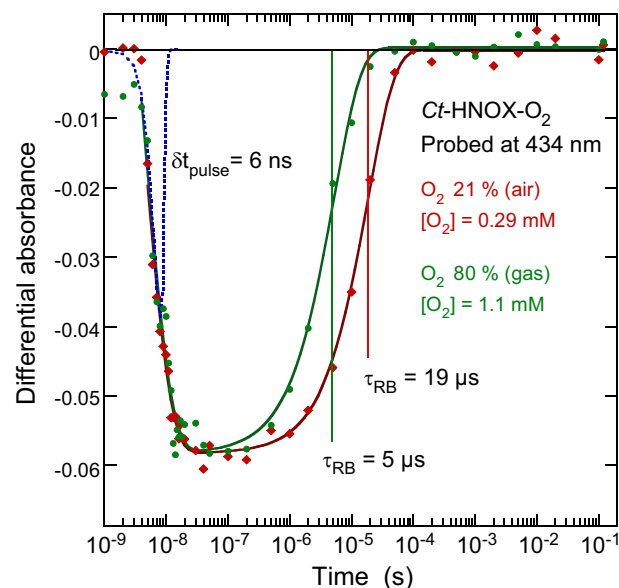


Fig. 4 Dynamics of O₂ rebinding to *Ct* H-NOX in the ns to 0.1 s time scale.

The dynamics was probed at 434 nm in the presence of 21% O₂ and ~80% O₂ in the gas phase. In the first case, the sample cell was open to the air. In the second case pure O₂ (Air Product) was injected into the open cell. The kinetics were fitted to the sum of two exponential components. The first fast component ($\tau_1 = \sim 4$ ns) corresponds to the rise of the signal (leading edge of the pulse). The second exponential is assigned to O₂ bimolecular rebinding from solution because its time constant depends on O₂ concentration ($\tau_2 = 19$ and 5 μ s). The profile of the 6-ns gaussian pulse is indicated by the blue dotted curve.

bimolecular rebinding proceeds from solution. We measured the dynamics of O₂ rebinding after its photodissociation from ferrous *Ct* H-NOX in the ns- μ s-ms time scale in the presence of 21% O₂ and 80% O₂ in gas phase (Fig. 4). The kinetics was monitored at the Soret absorption wavelength of the ferrous 5-c ferrous heme (434 nm) in order to follow its transition. An immediate negative absorption change occurred exactly as probed in the ps-ns time range, which confirms the decrease of the absorption coefficient of the 5-c ferrous heme after O₂ dissociation. Due to the time resolution (6 ns), the fast picosecond components of geminate rebinding of O₂ cannot be observed here. Importantly, we note that the measured kinetics of all 6-c Fe²⁺-O₂ heme proteins probed at 434 nm disclose a positive induced absorbance^{26,30,31,41,42} contrarily to the present case.

After the initial absorbance decay ($\tau_1 = 4$ ns) determined by the pulse shape (Gaussian curve in Fig. 4), the relaxation from heme distortion is completed within the time resolution <6 ns. Subsequently, only one exponential component could be identified, whose time constant depends on the O₂ concentration: $\tau_{RB} = 19$ μ s at [O₂] = 0.26 mM and $\tau_{RB} = 5$ μ s at [O₂] = 1.1 mM. This dependence allows to assign the transition to O₂ bimolecular rebinding from the solution, whose association rate can thus be calculated: $k_{on} = (1.9 \pm 0.2) \times 10^8$ M⁻¹ s⁻¹ (at 20 °C). This value is ~14 times larger than that measured by using 6-c Fe²⁺-CO *Ct* H-NOX as the initial species to be photodissociated¹⁵ (avoiding mixed kinetics due to the simultaneous presence of CO and O₂) and is ~4 times larger than that measured by stopped-flow (0.43×10^8 M⁻¹ s⁻¹)¹³. This very high rate indicates a diffusion controlled O₂ binding from the solution and the absence of a steric barrier. Because no other transitions were observed before or after, we concluded that O₂ binding from the solution induces the distortion of the heme faster than 5 μ s. The time constant of this

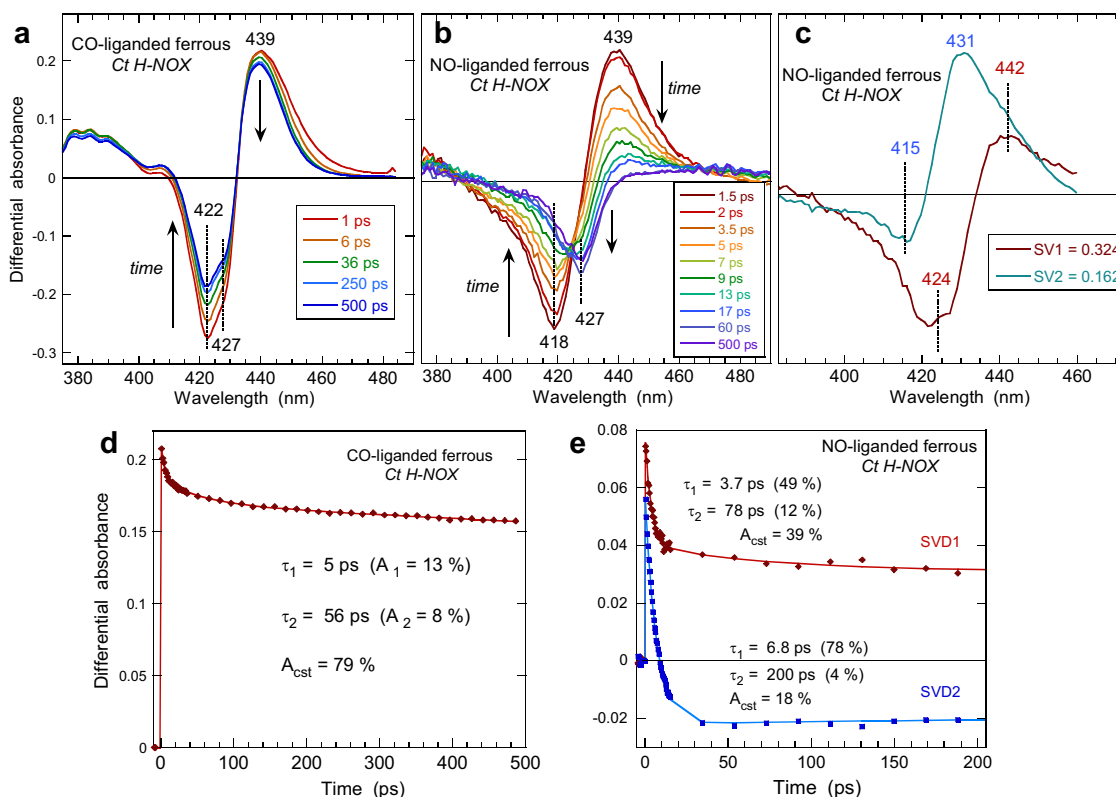


Fig. 5 Dynamics in CO-liganded and NO-liganded ferrous Ct H-NOX. Transient difference absorption spectra after the photodissociation of CO (**a**) and NO (**b**) from ferrous Ct H-NOX at increasing time delay ($\lambda_{\text{ex}} = 564 \text{ nm}$). (**c**) Spectral components from Singular Value Decomposition analysis of the time-wavelength data matrix of Ct H-NOX-NO. Associated kinetic components together with time constants for CO (**d**) and NO (**e**). Kinetics were fitted to the sum of two exponential terms with relative amplitudes A_i and a constant term A_{cst} (Supplementary Table S4).

allosteric transition is in the range of that measured for sGC (1–50 μs)⁴³.

Heme structural distortion change induced by other diatomics.

For all O_2 -binding proteins studied to date^{26,30,31,42}, a well-defined induced absorption band due to 5-c ferrous heme is present after O_2 dissociation and evolves with the bleaching when O_2 rebinds, contrarily to the present case, confirming that a fast structural change of the 5-c ferrous heme occurs in Ct H-NOX- O_2 . This result led us to compare the behavior of Ct H-NOX- O_2 with the diatomics CO and NO which both bind to the ferrous heme, and to measure the transient spectra in the same conditions (Fig. 5). After the photo-dissociation of CO, intense bleaching appeared centered at 422 nm (6-c heme—CO disappears) with a shoulder at 427 nm and an induced absorption at 439 nm (5-c heme appears). The transient spectra correspond to the difference equilibrium one (Supplementary Fig. S1b), except the shoulder (427 nm) present at the same wavelength as the bleaching induced after O_2 dissociation (Fig. 2a) but absent in the case of ferric heme (Fig. 3a). Thus, after the dissociation of CO two different conformational states of the heme are immediately formed which remain within similar proportions during 500 ps, contrarily to O_2 . The same relaxed heme conformation is also generated but in a much lower proportion than in the case O_2 as indicated by the large induced absorption remaining at 439 nm for CO but absent for O_2 . The associated kinetics (Fig. 5d) were fitted to the sum of two exponential decays: the first one ($\tau_1 = 5 \text{ ps}$) is assigned to excited states relaxation (small shift of the isosbestic point at 410 nm from 1 to 6 ps), whereas the second term ($\tau_2 = 56 \text{ ps}$) is due to fast CO geminate rebinding accounting for 8% of

the total amplitude. The constant term $A_{\text{cst}} = 79\%$ is due to slower bimolecular CO rebinding in the μs – ms time range. This kinetics is similar to those measured for the cognate H-NOX sensor from *Clostridium botulinum* and for guanylate cyclase⁴⁴.

The behavior of ferrous Ct H-NOX bound with NO (Fig. 5b) appeared intermediate between the CO- and the O_2 -bound sensor. The photodissociation of NO induced a bleaching centered at 418 nm (6-c heme—NO disappeared) and a well-defined induced absorption at 439 nm (5-c heme appeared) similarly with CO. The transient spectrum at +1.5 ps corresponds to the difference equilibrium one (Supplementary Fig. S1c) and NO geminately rebinds to the 5-c heme in the first 20 ps. Contrarily to CO, second bleaching develops at 427 nm (absent at 1.5 ps) while the induced absorption at 439 nm, due to 5-c heme, rapidly decreases. Remarkably, there is a large shift of the isosbestic point (~ 430 – 440 nm). Similarly with O_2 , two processes take place, namely the NO geminate rebinding and the relaxation of the distorted 5-c ferrous heme to a new conformational state. However, contrarily to O_2 , an induced absorption appears at 439 nm due to the unrelaxed dissociated 5-c heme (Fig. 5b). Here also, we discarded the hypothesis of photo-oxidation since no induced absorption appeared at 391 nm, as observed for ferric Ct H-NOX-NO (Fig. 3).

The two bleaching negative parts are well separated, allowing to resolve the entangled and evolving spectral contributions of both processes by SVD analysis. The SVD1 spectrum (Fig. 5c) corresponds to the heme structural relaxation and comprises an induced absorption (442 nm) because its initial decay is slower than that of O_2 . The SVD2 spectrum clearly corresponds to the steady-state difference (Supplementary Fig. S1c) but with a slight shift of the maximum of the positive band (436 nm). In the

transient SVD spectrum, there is a minor contribution of the 4-coordinate heme⁴³ due to the photo-dissociation of a small proportion of 5-c NO-heme (shoulder at 398 nm in Fig. S1c) preexisting together with 6-c heme. The presence of both species in various proportions is well known^{7,8,16} for all H-NOX sensors and is negligible for *Ct* H-NOX.

Like for other heme proteins, the NO geminate rebinding appears bi-exponential (Fig. 5e) with time constants close to those observed for globins⁴⁴ (Supplementary Table S4). The heme relaxation proceeds through two exponential phases, the fastest one ($\tau_1 = 3.7$ ps) is due to vibrational excited states decay³⁷ whereas the second one ($\tau_{R2} = 78$ ps) is assigned to heme structural relaxation to an equilibrium state. It is similar to that measured for O₂. The excitation in the Q-band that we used (564 nm) allows to minimize the thermal energy to be dissipated by the heme compared to a Soret excitation³⁹. The heme structural relaxation ($\tau_{R2} = 78$ ps) appears as a consequence of NO dissociation, not of electronic excitation, and could have been hardly detected in the absence of spectral resolution (which is the case when using an large open band detection)³⁹.

All together the present results signify that the conformation of *Ct* H-NOX ferrous heme transiently changes, but not its redox state, with an absorption spectrum different than the ground 5-c ferrous state. The lower absorption coefficient can originate from a change of orbitals overlap due to a change of heme distortion. The remarkably different evolution of the transient spectra depending on the diatomics, but with the presence of a heme relaxed species in all three cases, confirms that a fast structural change of the 5-c ferrous heme occurs for *Ct* H-NOX when O₂ dissociates.

Discussion

The spectral evolution triggered by photodissociation of diatomics described here has never been observed previously in other O₂-binding heme proteins, for which a positive induced absorption was always measured upon O₂ dissociation (Supplementary Table S3), contrarily to *Ct* H-NOX. These results reveal that the dissociation of diatomics from ferrous *Ct* H-NOX induces a spontaneous structural change of the heme, but in different proportions depending on the diatomics as follows: CO < NO < O₂ (Supplementary Table S5). Immediately (~1 ps) after ligand dissociation, the ferrous 5-c heme macrocycle could be supposedly in the 6-c structural conformation it had before dissociation (excepting the instantaneous motion of Fe out of the

heme plane)⁴⁵, but this is not the case: the transient absorption data imply that the dissociated heme adopts fastly (<1 ps) a new 5-c conformation which has a strong influence on its electronic structure, impacting its absorption coefficient. The reverse conformational change of the heme takes place upon O₂ binding. Let us remind that the heme in steady-state crystal structures is highly distorted in the 6-c Fe(II)-O₂ state¹⁷ (tensed state) and flattened in the 5-c Fe(II) one (relaxed state). The distortion comprises both saddling and ruffling components^{5,20,21}. Since in other heme proteins the O₂ binding does not induce a so strong distortion of the heme⁵, the protein environment in *Ct* H-NOX is responsible of the unique heme distortion upon O₂ binding, implying that specific interactions take place between O₂ and distal side-chains.

The relaxation observed after NO dissociation implies that NO also induces a tensed conformation but in a lower amount. The 6-c state is even less distorted when CO is bound, but still exists and relaxes also immediately upon CO dissociation. All three ligands O₂, NO, and CO bound to *Ct* H-NOX induce heme distortion, but to different extents as quantified by the ratio of the two SVD components associated with heme structural relaxation and ligand rebinding (Supplementary Table S5). Remarkably, the steady-state structures bound with the diatomics reveals lower distortions in the presence of CO and NO¹⁷. This difference fully agrees with the relative amplitudes of SVD structural relaxation components measured for the three species, which are associated with lower energy states for CO and NO. Immediately after O₂ dissociation, the heme conformation is out of equilibrium, in a higher energy state, and can access the relaxed 5-c equilibrium state without energy barrier, which translates to fast picosecond kinetics, whereas a lower energy difference (also without barrier) translates to slower relaxations in the case of NO.

The heme relaxed state can be produced when the heme is electronically excited. This observation suggests that a mixture of distorted and relaxed 5-c ferrous hemes may preexist at equilibrium, which is displaced by ligand binding. Electronic excitation allows the distorted heme to relax and changes the relative populations, the initial equilibrium being restored in a time scale larger than 5 ns.

The heme distortion influences the molecular orbitals⁴⁶ and must alter the absorption coefficient. We calculated the Soret absorption spectrum of the relaxed 5-c ferrous heme from the transient spectrum after electronic excitation (Fig. 6a) by subtracting the non excited contribution from the transient spectrum

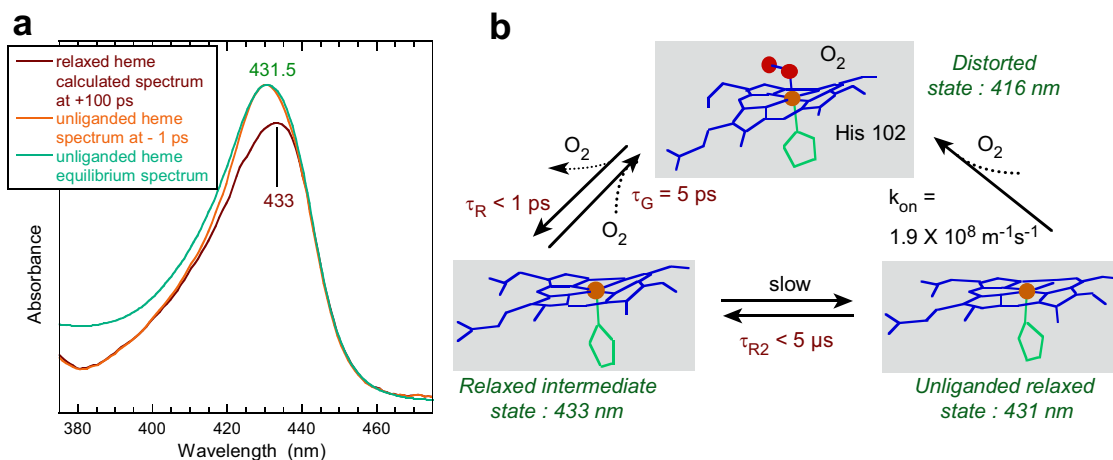


Fig. 6 Spectroscopic fingerprint and model. **a** Calculated spectrum of the relaxed 5-c ferrous heme of *Ct* H-NOX at +100 ps after O₂ dissociation (red) compared with the spectrum of the unliganded 5-c heme before excitation (−1 ps, orange) and with the steady-state spectrum of the same sample (green). In the latter spectrum the increased absorbance below ~400 nm is due to the reductant dithionite which is less consumed. **b** Allosteric equilibrium based on heme distortion in the *Ct* H-NOX sensor.

at +100 ps. The relaxed heme after photoexcitation has a Soret maximum shifted to 433 nm and a lower absorption coefficient compared to its unliganded equilibrium state, revealing changes in orbitals due to the change in heme distortion. Apart from the UV-visible spectrum, the heme redox potential is another electronic property which is influenced^{20,22} and could be important for *Ct* H-NOX function.

For all three ligands CO, NO, and O₂ the heme relaxation takes place immediately after their dissociation (picosecond) and the produced 5-c heme spectrum not only differs from that at the equilibrium 5-c unliganded state, but also differs from the 5-c spectrum would be if the heme kept the ligand-bound conformation after dissociation. Time-resolved absorption has previously shown that the spectrum of the bacterial O₂-sensor FixL after dissociation differs from the spectrum of the 5-c unliganded equilibrium state, being blue-shifted⁴². For FixL (with a tertiary fold different from *Ct* H-NOX), the 5-c heme conformation immediately after ligand dissociation is the same as in the 6-c liganded state, but different from the 5-c unliganded state. Contrastingly, for *Ct* H-NOX the heme conformation changes immediately after dissociation and is not the same as in the 5-c unliganded equilibrium state (Fig. 6). However, a common feature of FixL and *Ct* H-NOX is the difference of heme response between the three diatomics in the order CO < NO < O₂, revealed by time-resolved Raman spectroscopy for FixL⁴⁷. In the present study, this difference of reactivity is translated into the ratio of SVD amplitudes (γ_{SVD}) of the transient spectral components (Supplementary Table S5). However, the allosteric mechanisms in FixL and *Ct* H-NOX sensors are based on different properties and different interactions between heme and protein, which reflect their adaptation to different environments.

To summarize concisely, our time-resolved spectroscopic data demonstrates that heme distortion is released in <1 ps after O₂ detachment. This dynamics of the heme (so far not described) controls the allosteric equilibrium in the *Ct* H-NOX sensor. The dynamics of heme distortion appears as another mechanism for triggering allostery in heme proteins, in contrast with hemoglobin and guanylate cyclase, in which the primary structural events are respectively the motion of the proximal histidine linked to the heme and the rupture of the iron-histidine bond.

Methods

Preparation of the samples. The sample of bacterial H-NOX domain from *Caldanaerobacter tencongensis* comprising the first 191 amino-acids (*Ct* H-NOX), homologous to the heme domain of sGC was overexpressed⁴. The protein was purified in the O₂-liganded ferrous state (as verified by its absorption spectrum, Supplementary Fig. S1a), kept at -80 °C in triethanolamine (TEA) buffer supplemented with 5% glycerol and was thawed immediately before use.

For all steady-state and time-resolved absorption measurements, quartz cells with an optical path of 1 mm were always used (Hellma, 110-QX). The steady-state spectrometer is a Shimadzu UV-1700. All measurements were performed at 20 °C. The absorbance of the samples was in the range 0.5–0.8 at the Soret maximum for 1-mm path length.

To measure the spectra of ferrous *Ct* H-NOX coordinated with O₂ we used the protein as purified. An aliquot of *Ct* H-NOX (120 μ L at 50 μ M) in a buffer (50 mM Tris-HCl pH 7.5) was placed in a cell kept in equilibrium with air, corresponding to 290 μ M of O₂ in the aqueous phase at 20 °C. We have verified that its spectrum is identical to that obtained by reducing the ferric protein (see below) and exposing it to air. The absorption spectrum of the samples was verified at each step of the preparation and after each time-resolved experiment.

Preparation of ferrous *Ct* H-NOX liganded with NO or CO. An aliquot of *Ct* H-NOX (120 μ L at 50 μ M) in a buffer (50 mM Tris-HCl pH 7.5) was degassed directly in the spectroscopic cell sealed with a rubber stopper. Thorough degassing was obtained by means of four successive cycles of vacuum (0.3 mbar) and purging with pure argon (1.3 bar) for 10 min between each cycle. Then, 10 μ L of degassed sodium dithionite (Na₂S₂O₄) were added with a syringe (1 mM final concentration) and the cell was heated 5 min at 50 °C to facilitate O₂ dissociation. Dithionite eliminated remaining traces of O₂. The fully reduced unliganded *Ct* H-NOX (Soret

band maximum at 432 nm, Supplementary Fig. S1) was nitrosylated by introducing 10% NO gas (diluted in nitrogen) in the vacuumed cell, at a final pressure of ~1.3 bar, yielding 200 μ M NO in the aqueous phase at 20 °C. Rigorous airtightness of the cell was ensured by putting vacuum grease at the top of the first stopper and then the second stopper in silicone. For preparing the CO-liganded protein the same procedure was used, but introducing 100% CO gas in the cell.

Preparation of ferric *Ct* H-NOX. The as-prepared sample of *Ct* H-NOX-O₂ (~40 μ M, 120 μ L) was placed in a spectroscopic cell and thoroughly degassed with repeated cycles of vacuuming and purging with argon. Then the sample, still O₂-liganded, was oxidized by mild heating (65 °C for 20 min). The Soret appeared at 409 nm with the presence of a small absorption band centered at 630 nm (Supplementary Fig. S1d). The cell was again degassed and NO gas (at 10% in N₂ yielding 200 μ M of NO in solution) was introduced into the cell. The Soret band shifted to 424.5 nm with well-defined Q-bands at 538–572 nm.

Picosecond to nanosecond time-resolved absorption spectroscopy. The photodissociation of CO, NO, and O₂ was achieved with an excitation pulse at 564 nm, in the Q-band absorption of the heme, whose duration was ~50 fs with a repetition rate of 30 Hz. The energy of one pump pulse (~0.1 μ J) does not damage the sample, which was continuously moved perpendicularly to the beams to ensure sample renewal between pulses. The probe pulse (<50 nJ, 375–500 nm) was part of a broad band continuum generated by focusing a 620-nm pulse (~3 μ J, 50 fs) in a 1-cm water cell. Both pump and probe pulses (respective beam waists of ~150 μ m and ~100 μ m) were focused and overlapped in the sample cell. The optical path length of the cell was 1 mm. After the sample cell, the probe beam is directed into a monochromator (model H25, Jobin Yvon) equipped with a nitrogen-cooled charge-coupled detector (EG&G Princeton Applied Research). The transient Soret absorption was recorded as a function of time delay between pump and probe pulses. Up to 40 scans were recorded and averaged with a dwell time of 1 s for each individual transient spectrum.

Transient spectra and kinetics were simultaneously recorded to generate a time-wavelength data matrix $\Delta A(\lambda, t)$. Analysis of the data was performed by singular value decomposition (SVD) of this time-wavelength matrix^{32,37} which allows the separation of entangled transient spectral components. In brief, the experimental data matrix $\Delta A(\lambda, t)$ composed of differential absorption spectra at different time delays was decomposed according to

$$\Delta A(\lambda, t) = \Delta A^{\text{SVD}}(\lambda) \cdot S \cdot K^{\text{SVD}}(t)$$

giving the matrix $\Delta A^{\text{SVD}}(\lambda)$ of orthogonal spectral components and the matrix $K^{\text{SVD}}(t)$ of associated kinetics, weighted by the singular values S_i (elements of the diagonal matrix S)³². This procedure (home-written software) allows the identification of processes associated with particular spectral components. The SVD kinetic components were fitted to the sum of a minimum number of exponential components. Alternatively, kinetics were also performed at particular wavelengths of the raw data matrix. The temperature of the samples was 20 °C for all experiments.

A reference pulse (same energy and spectrum as the probe pulse) is recorded simultaneously with the probe, allowing to calculate the absolute absorbance for each pixel and time delay, and thus the absolute transient spectra. There is always a contribution from the non photo-excited species, which can be removed by subtracting the spectrum before excitation, with a weighting coefficient, from the spectrum at a given time delay. We could thus obtain the pure absolute spectrum of the relaxed heme (Fig. 6a) after photo-excitation, whereas the Figs. 2–5 present difference transient spectra to clearly show the change.

Nanosecond to second time-resolved absorption spectroscopy. For time-resolved absorption in the extended time-range nanosecond to second, we have used the home-built spectrophotometer at Institut de Biologie Physico-Chimique (Paris). This system comprises two lasers which are electronically synchronized⁴⁸. The dissociating pulse is provided by the second harmonic (532 nm) of a Nd/YAG laser and has a duration of 6 ns. The probing pulses (duration 5 ns) were provided by a tunable optical parametric oscillator pumped by the third harmonic of another Nd/YAG laser. The sample cell compartment and light collection design allowed us to record signal variations of absorbance $\Delta A/A$ as low as 10⁻⁵. The pump and probe pulses (10 μ J) were not focused into the sample cell but spread over the surface of the sample (~1 cm²) by means of a bundle of optical fibers⁴⁸. The kinetics of differential absorption changes were probed at particular wavelengths by tuning the optical parametric oscillator. Up to twelve scans were averaged for each kinetics. The time delay after the dissociating pulse was changed linearly from 1 to 30 ns, then was changed with a logarithmic progression from 30 ns to 1 s. The kinetics at a particular wavelength was globally fitted to the sum of a minimum number of exponential components. The temperature of the samples was 20 °C.

Data availability

The authors declare that all data supporting the findings of this study are included in the main manuscript file or Supplementary Information or are available from the corresponding author upon request.

Received: 25 September 2020; Accepted: 5 February 2021;

Published online: 05 March 2021

References

1. Shimizu, T. et al. Gaseous O₂, NO, and CO in signal transduction: structure and function relationships of heme-based gas sensors and heme-redox sensors. *Chem. Rev.* **115**, 6491–6533 (2015).
2. Martínková, M., Kitanishi, K. & Shimizu, T. Heme-based globin-coupled oxygen sensors: linking oxygen binding to functional regulation of diguanylate cyclase, histidine kinase, and methyl-accepting chemotaxis. *J. Biol. Chem.* **288**, 27702–27711 (2013).
3. Iyer, L. M., Anantharaman, V. & Aravind, L. Ancient conserved domains shared by animal soluble guanylyl cyclases and bacterial signaling proteins. *BMC Genomics* **4**, 5 (2003).
4. Nioche, P. et al. Femtomolar sensitivity of a NO sensor from *Clostridium botulinum*. *Science* **306**, 1550–1553 (2004).
5. Pellicena, P., Karow, D. S., Boon, E. M., Marletta, M. A. & Kuriyan, J. Crystal structure of an oxygen-binding heme domain related to soluble guanylate cyclases. *Proc. Natl Acad. Sci. USA* **101**, 12854–12859 (2004).
6. Ignarro, L. J., Cirino, G., Casini, A. & Napoli, C. Nitric oxide as a signaling molecule in the vascular system: an overview. *J. Cardiovasc. Pharm.* **34**, 879–886 (1999).
7. Karow, D. S. et al. Spectroscopic characterization of the soluble guanylate cyclase-like heme domains from *Vibrio cholerae* and *Thermoanaerobacter tengcongensis*. *Biochemistry* **43**, 10203–10211 (2004).
8. Boon, E. M. & Marletta, M. A. Ligand specificity of H-NOX domains: from sGC to bacterial NO sensors. *J. Inorg. Biochem.* **99**, 892–902 (2005).
9. Erbil, W. K., Price, M. S., Wemmer, D. E. & Marletta, M. A. A structural basis for H-NOX signaling in *Shewanella oneidensis* by trapping a histidine kinase inhibitory conformation. *Proc. Natl Acad. Sci. USA* **106**, 19753–19760 (2009).
10. Nisbett, L.-M. et al. NosP signaling modulates the NO/H-NOX-mediated multicomponent c-Di-GMP network and biofilm formation in *Shewanella oneidensis*. *Biochemistry* **58**, 4827–4841 (2019).
11. Xue, Y., Xu, Y., Liu, Y., Ma, Y. & Zhou, P. *Thermoanaerobacter tengcongensis* sp. nov., a novel anaerobic, saccharolytic, thermophilic bacterium isolated from a hot spring in Tengcong, China. *Int. J. Syst. Evol. Microbiol.* **51**, 1335–1341 (2001).
12. Fardeau, M. L. et al. Isolation from oil reservoirs of novel thermophilic anaerobes phylogenetically related to *Thermoanaerobacter subterraneus*: reassignment of *T. subterraneus*, *Thermoanaerobacter yonseiensis*, *Thermoanaerobacter tengcongensis* and *Carboxydibrachium pacificum* to *Caldanaerobacter subterraneus* as four novel subspecies. *Int. J. Syst. Evol. Microbiol.* **54**, 467–474 (2004).
13. Wu, G., Liu, W., Berka, V. & Tsai, A.-L. H-NOX from *Clostridium botulinum*, like H-NOX from *Thermoanaerobacter tengcongensis*, binds oxygen but with a less stable oxyferrous heme intermediate. *Biochemistry* **54**, 7098–7109 (2015).
14. Weinert, E. E., Phillips-Piro, C. M., Tran, R., Mathies, R. A. & Marletta, M. A. Controlling conformational flexibility of an O₂-binding H-NOX domain. *Biochemistry* **50**, 6832–6840 (2011).
15. Boon, E. M., Huang, S. H. & Marletta, M. A. A molecular basis for NO selectivity in soluble guanylate cyclase. *Nat. Chem. Biol.* **1**, 53–59 (2005).
16. Tsai, A.-L., Berka, V., Martin, E. & Olson, J. S. A “sliding scale rule” for selectivity among NO, CO, and O₂ by heme protein sensors. *Biochemistry* **51**, 172–186 (2011).
17. Hespen, C. W., Bruegger, J. J., Phillips-Piro, C. M. & Marletta, M. A. Structural and functional evidence indicates selective oxygen signaling in *Caldanaerobacter subterraneus* H-NOX. *ACS Chem. Biol.* **11**, 2337–2346 (2016).
18. Cross, R., Aish, J., Paston, S. J., Poole, R. K. & Moir, J. W. B. Cytochrome *c* from *Rhodobacter capsulatus* confers increased resistance to nitric oxide. *J. Bacteriol.* **182**, 1442–1447 (2000).
19. Negrerie, M. Iron transitions during activation of allosteric heme proteins in cell signaling. *Metallomics* **11**, 868–893 (2019).
20. Olea, C., Boon, E. M., Pellicena, P., Kuriyan, J. & Marletta, M. A. Probing the function of heme distortion in the H-NOX family. *ACS Chem. Biol.* **3**, 703–710 (2008).
21. Tran, R., Boon, E. M., Marletta, M. A. & Mathies, R. A. Resonance Raman spectra of an O₂-binding H-NOX domain reveal heme relaxation upon mutation. *Biochemistry* **48**, 8568–8577 (2009).
22. Olea, C., Kuriyan, J. & Marletta, M. A. Modulating heme redox potential through protein-induced porphyrin distortion. *J. Am. Chem. Soc.* **132**, 12794–12795 (2010).
23. Kanematsu, Y., Kondo, H. X., Imada, Y. & Takano, Y. Statistical and quantum-chemical analysis of the effect of heme porphyrin distortion in heme proteins: differences between oxidoreductases and oxygen carrier proteins. *Chem. Phys. Lett.* **710**, 108–112 (2018).
24. Shelnett, J. A. et al. Nonplanar porphyrins and their significance in proteins. *Chem. Soc. Rev.* **27**, 31–41 (1998).
25. Karunakaran, V., Benabbas, A., Youn, H. & Champion, P. M. Vibrational coherence spectroscopy of the heme domain in the CO-sensing transcriptional activator CooA. *J. Am. Chem. Soc.* **133**, 18816–18827 (2011).
26. Ramos-Alvarez, C. et al. Reactivity and dynamics of H₂S, NO, and O₂ interacting with hemoglobins from *Lucina pectinata*. *Biochemistry* **52**, 7007–7021 (2013).
27. Negrerie, M., Bouzahir, L., Martin, J.-L. & Liebl, U. Control of nitric oxide dynamics by guanylate cyclase in its activated state. *J. Biol. Chem.* **276**, 46815–46821 (2001).
28. Champagne, D. E., Nussenzweig, R. H. & Ribeiro, J. M. Purification, partial characterization, and cloning of nitric oxide-carrying heme proteins (nitrophorins) from salivary glands of the blood-sucking insect *Rhodnius prolixus*. *J. Biol. Chem.* **270**, 8691–8695 (1995).
29. Andersen, J. F. et al. Nitric oxide binding and crystallization of recombinant nitrophorin I, a nitric oxide transport protein from the blood-sucking bug *Rhodnius prolixus*. *Biochemistry* **36**, 4423–4428 (1997).
30. Andrew, C. R. et al. The dynamics behind the affinity: controlling heme-gas affinity via geminate recombination and heme propionate conformation in the NO carrier cytochrome *c*. *ACS Chem. Biol.* **11**, 3191–3201 (2016).
31. Ye, X., Demidov, A. & Champion, P. M. Measurements of the photodissociation quantum yields of MbNO and MbO₂ and the vibrational relaxation of the six-coordinate heme species. *J. Am. Chem. Soc.* **124**, 5914–5924 (2002).
32. Press, W. H., Flannery, B. P., Teukolsky, S. A. & Vetterling, W. T. *Numerical Recipes: The Art of Scientific Computing*. (Cambridge University Press, New York, 1989).
33. Cao, W., Christian, J. F., Champion, P. M., Rosca, F. & Sage, J. T. Water penetration and binding to ferric myoglobin. *Biochemistry* **40**, 5728–5737 (2001).
34. Negrerie, M. et al. Geminate recombination of nitric oxide to endothelial nitric oxide-synthase and mechanistic implications. *J. Biol. Chem.* **274**, 24694–24702 (1999).
35. Rahaman, M. M. et al. Cytochrome *b5* reductase 3 modulates soluble guanylate cyclase redox state and cGMP signaling. *Circ. Res.* **121**, 137–148 (2017).
36. Ye, X. et al. Investigations of heme protein absorption line shapes, vibrational relaxation, and resonance Raman scattering on ultrafast time scales. *J. Phys. Chem. A* **107**, 8156–8165 (2003).
37. Negrerie, M., Cianetti, S., Vos, M. H., Martin, J.-L. & Kruglik, S. G. Ultrafast heme dynamics in ferrous versus ferric cytochrome *c* studied by time-resolved resonance Raman and transient absorption spectroscopy. *J. Phys. Chem. B* **110**, 12766–12781 (2006).
38. Wang, W. et al. Femtosecond multicolor pump–probe spectroscopy of ferrous cytochrome *c*. *J. Phys. Chem. B* **104**, 10789–10801 (2000).
39. Sun, Y. et al. Kinetic control of O₂ reactivity in H-NOX domains. *J. Phys. Chem. B* **120**, 5351–5358 (2016).
40. Chauvet, A. P., Agarwal, R., al Haddad, A., van Mourik, F. & Cramer, W. A. Photo-induced oxidation of the uniquely liganded heme *f* in the cytochrome *b₆f* complex of oxygenic photosynthesis. *Phys. Chem. Chem. Phys.* **18**, 12983–12991 (2016).
41. Wang, Y., Baskin, J. S., Xia, T. & Zewail, A. H. Human myoglobin recognition of oxygen: dynamics of the energy landscape. *Proc. Natl Acad. Sci. USA* **101**, 18000–18005 (2004).
42. Liebl, U., Bouzahir-Sima, L., Negrerie, M., Martin, J.-L. & Vos, M. H. Ultrafast ligand rebinding in the heme domain of the oxygen sensors FixL and Dos: general regulatory implications for heme-based sensors. *Proc. Natl Acad. Sci. USA* **99**, 12771–12776 (2002).
43. Yoo, B. K., Lamarre, I., Martin, J. L., Rappaport, F. & Negrerie, M. Motion of proximal histidine and structural allosteric transition in soluble guanylate cyclase. *Proc. Natl Acad. Sci. USA* **112**, E1697–E1704 (2015).
44. Yoo, B.-K. et al. Picosecond to second dynamics reveals a structural transition in *Clostridium botulinum* NO-sensor triggered by the activator BAY-412272. *ACS Chem. Biol.* **7**, 2046–2054 (2012).
45. Kruglik, S. G. et al. Picosecond primary structural transition of the heme is retarded after nitric oxide binding to heme proteins. *Proc. Natl Acad. Sci. USA* **107**, 13678–13783 (2010).
46. Liptak, M. D., Wen, X. & Bren, K. L. NMR and DFT investigation of heme ruffling: functional implications for cytochrome *c*. *J. Am. Chem. Soc.* **132**, 9753–9763 (2010).
47. Kruglik, S. G., Lambry, J.-C., Martin, J.-L., Vos, M. H. & Negrerie, M. Sub-picosecond Raman spectrometer for time-resolved studies of structural dynamics in heme proteins. *J. Raman Spectrosc.* **42**, 265–275 (2011).

48. Beal, D., Rappaport, F. & Joliot, P. A new high-sensitivity 10-ns time-resolution spectrophotometric technique adapted to in vivo analysis of the photosynthetic apparatus. *Rev. Sci. Instrum.* **70**, 202–207 (1999).

Acknowledgements

P.N. was supported by an Avenir starting grant, Region Ile-de-France under a CODDIM contract, an INSERM-Paris Descartes University Chaire mixte. O.N.P. was supported by an "Initiative Doctorale Interdisciplinaire" PhD fellowship from Université Paris-Saclay.

Author contributions

M.N. conceived and designed the research. P.N. produced and purified the protein. I.L. and O.N.P. performed biochemical analysis. O.N.P., B.-K.Y., and J.S. performed time-resolved measurements. M.N., O.N.P., and B.-K.Y. analyzed the data. M.N. and O.N.P. prepared the figures and wrote the manuscript. All authors approved the final version of the manuscript.

Competing interests

The authors declare no competing interests.

Additional information

Supplementary information The online version contains supplementary material available at <https://doi.org/10.1038/s42004-021-00471-9>.

Correspondence and requests for materials should be addressed to M.N.

Reprints and permission information is available at <http://www.nature.com/reprints>

Publisher's note Springer Nature remains neutral with regard to jurisdictional claims in published maps and institutional affiliations.



Open Access This article is licensed under a Creative Commons Attribution 4.0 International License, which permits use, sharing, adaptation, distribution and reproduction in any medium or format, as long as you give appropriate credit to the original author(s) and the source, provide a link to the Creative Commons license, and indicate if changes were made. The images or other third party material in this article are included in the article's Creative Commons license, unless indicated otherwise in a credit line to the material. If material is not included in the article's Creative Commons license and your intended use is not permitted by statutory regulation or exceeds the permitted use, you will need to obtain permission directly from the copyright holder. To view a copy of this license, visit <http://creativecommons.org/licenses/by/4.0/>.

© The Author(s) 2021